

Cite this: DOI: 00.0000/xxxxxxxxxx

Collective dynamics of active dumbbells near circular obstacle[†]

Chandranshu Tiwari^{*a}, and Sunil P. Singh^bReceived Date
Accepted Date

DOI: 00.0000/xxxxxxxxxx

In this article, we present the collective dynamics of active dumbbells in the presence of a static circular obstacle using Brownian dynamics simulation. The active dumbbells aggregate on the surface of a circular obstacle beyond a critical radius ($R_c^o \approx 10$). The aggregation is non-uniform along the circumference, and the aggregate size increases with the activity (Pe) and the curvature radius (R_o). The dense aggregate of active dumbbells displays persistent rotational motion with a certain angular speed, which linearly increases with the activity. Further, we show the strong polar ordering of the active dumbbells within the aggregate. The polar ordering exhibits a long-range correlation, with the correlation length corresponding to the aggregate size. Additionally, we show that the residence time of an active dumbbell on the obstacle surface grows rapidly with area fraction due to many-body interactions that lead to a slowdown of the rotational diffusion. The article further considers the dynamical behavior of a tracer particle in the solution of active dumbbells. Interestingly, the speed of the passive tracer particle displays a crossover from monotonically decreasing to increasing with the tracer particle's size upon increasing the dumbbells' speed. Furthermore, the effective diffusion of the tracer particle displays the non-monotonic behavior with area fraction; the initial increase of the diffusivity is followed by a decrease for larger area fraction.

1 Introduction

The collection of micro-swimmers such as bacteria, algae, amoeba, sperms, etc., exhibit rich collective dynamics in bulk, and the proximity of solid interface^{1–13}. Notably, phase separation at low density^{14,15}, circular motion, spontaneous vortex formation in microfluidic devices^{16–18}, bacterial turbulence at low Reynolds number^{19–21}, giant density fluctuations^{6,13}, formation of a periodic array of vortices of bacterial colonies²², self-organization of unicellular organisms in fruiting bodies¹⁴, biofilm formation, etc^{23,24}. Dynamics of such microswimmers in confined environments have attracted immense research interest due to plenty of non-intriguing physical behavior observed, viz., the propensity to swim upstream, helical or chaotic trajectories of motion, tumbling motion^{25–30}, rectification of swimming speed, and its aggregation⁷. Furthermore, numerous experiments have revealed aggregation of micro-swimmers on the solid interface that leads to segregation of slow-moving ordered phase (near surface) and fast-moving random phase (bulk); such aggregate also displays intriguing rotational motion^{16,17,21,22}.

Some of the characteristic features of such a complex system

are successfully captured in the simple analytical and simulation models^{1,9,18,43–59}. The ellipsoid-like, elongated particles are often treated as a model system for *bacterial suspensions* in the literature for the study of the motility-induced phase separation (MIPS)^{49,60,61}, aggregation on the solid interface^{1,62}, collective dynamics induced by steric interactions, vortex formation in confined environment^{16,17}, the role of fluid flow^{51,63–65}, etc. The active dumbbell particle can be entrapped around static circular obstacles by the orbital motion; the mechanism behind entrapment may be hydrodynamic in nature.^{66–69} Additionally, the large aggregate of spherical particles in certain parameter space spontaneously forms a vortex without any symmetry-breaking facets in the system^{70,71}. This emergent phenomenon purely appears from the bias of accepting the incoming particles around the rotating clusters^{70,71}. On the other hand, anisotropic-shaped self-propelled particles confined in the 2D geometry show interesting phenomena, such as the translation motion of the hedgehog structure and vortex formation of *Bacillus subtilis* bacterial suspension^{16,72}. Despite their relevance in understanding microbial dynamics in microfabricated structures and porous media, the characteristic features of collective dynamics of the elongated-shaped micro-swimmers in proximity to convex-shape static obstacles are still lacking^{16,70,73}.

Our work aims to present a comprehensive study of the collective dynamics of anisotropic-shaped active particles in the pres-

^a Department of Physics, Indian Institute Of Science Education and Research, Bhopal 462 066, Madhya Pradesh, India; E-mail: chandranshu21@iiserb.ac.in

^b Department of Physics, Indian Institute Of Science Education and Research, Bhopal 462 066, Madhya Pradesh, India; E-mail: spsingh@iiserb.ac.in

ence of a convex-shaped static obstacle in the two-dimension by exploiting over-damped Brownian dynamics simulations. The anisotropic-shaped active particles are modeled by connecting two disk-like monomers via a spring potential called active dumbbells. Furthermore, our work aims to provide the transport behavior of the tracer particle in the solution of active dumbbells. This can be qualitatively compared to the experimental work of the tracer particle's dynamics in the bacterial bath^{74–77}.

We demonstrate that the active dumbbells aggregate on the surface of the static obstacle only if the radius of the obstacle $R_o \geq 10$. The aggregation is non-uniform along the circumference and grows with the speed of the dumbbells and the obstacle's curvature radius R_o . Remarkably, these dense aggregates of active dumbbells exhibit fascinating collective dynamics on the static obstacle, displaying persistent rotational motion. The rotational motion can be clockwise or counter-clockwise; such motion is stable for a long time and appears spontaneously. Furthermore, our simulations demonstrate strong polar ordering of active dumbbells within the aggregate, where they align themselves on the surface in a spiral form.

The active dumbbells align on the surface at a certain angle, which is normal to the obstacle's surface. This angle decreases with the curvature radius and increases with the speed of the dumbbells. The polar ordering of the active dumbbells on the surface displays long-range ordering with the correlation length corresponding to the aggregate size. We elucidate the physical mechanism underlying the aggregation of dumbbells on the convex surface by computing the residence time. The residence time increases rapidly with the concentration of active dumbbells due to many-body interactions.

In another scenario, we consider a tracer particle free to move in response to the active force arising from the collision with the active dumbbells in the medium. Our findings indicate that the directed speed of larger-sized tracer particle surpasses that of smaller-sized ones and displays non-monotonic behavior. Furthermore, the effective diffusion of the tracer particle also displays the non-monotonic behavior with area fraction. The initial increase of the diffusivity is followed by a decrease upon increasing the area fraction, which is very different from the passive solution, where it monotonically decreases with the fraction.

The structure of the article is as follows: Section 2 discusses the simulation model of the active dumbbells and simulation parameters. The simulation results are given in Section 3, which further consists of four subsections. These subsections provide detailed insights into aggregation, orientational ordering, dynamics of active dumbbells, and dynamics of passive tracer particle within the active medium. The discussion and summary of the results are presented in the conclusion, Section 4.

2 Simulation Model

We model N_d polar active dumbbells representing anisotropic-shaped microswimmers in the two-dimensional box with periodic boundary conditions. Additionally, a disc-shaped static circular obstacle of radius R_o is embedded at the center of the simulation box. The active dumbbells comprise two identical monomers of

diameter σ connected by the harmonic potential U_s :

$$U_s = \sum_{i=1}^{N_d} \frac{k_s}{2} (|\mathbf{r}_{2i} - \mathbf{r}_{2i-1}| - l_0)^2, \quad (1)$$

where \mathbf{r}_{2i} and \mathbf{r}_{2i-1} are the position vectors of monomers of the i^{th} dumbbell, l_0 is the equilibrium bond length, and k_s is the spring constant, here i varies from $1, 2, \dots, N_d$. To avoid the overlap among various dumbbells, the excluded volume interaction is employed by truncated repulsive Lennard-Jones potential (LJ),

$$U_{LJ} = \sum_{i=1}^{2N_d-1} \sum_{j=i+1}^{2N_d} 4\epsilon \left[\left(\frac{\sigma}{r_{ij}} \right)^{12} - \left(\frac{\sigma}{r_{ij}} \right)^6 + \frac{1}{4} \right]. \quad (2)$$

The LJ potential for a given pair $U_{LJ} = 0$ for $r_{ij} \geq 2^{1/6}\sigma$, else given by above Eq.2, where $r_{ij} = |\mathbf{r}_i - \mathbf{r}_j|$ is the distance between a pair i and j , and ϵ is strength of LJ repulsion.

The interaction of monomers with the static circular obstacle is also employed via short-range LJ potential given in Eq. 2 if the distance between the monomer and the obstacle's wall is less than $2^{1/6}(\sigma/2)$ else they do not feel force from the obstacle.

The self-propulsion force f_a is imposed along the direction of the bond vector connecting tail to head monomers^{18,49}. Therefore active force on the i^{th} dumbbell is given as $\mathbf{F}_a^i = 2f_a\hat{\mathbf{n}}_i$, here f_a is the strength of active force and $\hat{\mathbf{n}}_i$ is the unit vector given by $\hat{\mathbf{n}}_i = \frac{\mathbf{r}_{2i} - \mathbf{r}_{2i-1}}{|\mathbf{r}_{2i} - \mathbf{r}_{2i-1}|}$.

The overdamped Langevin equation governs the equation of motion of a monomer,

$$\frac{\partial \mathbf{r}_i}{\partial t} = \frac{1}{\gamma_i} \left[-\nabla_i U_{LJ} - \nabla_i U_s + \mathbf{F}_w^i + f_a \hat{\mathbf{n}}_i \right] + \boldsymbol{\eta}_i^T, \quad (3)$$

where γ_i is the viscous drag, $\boldsymbol{\eta}_i^T$ is Gaussian white noise having zero mean, and its correlation is expressed in terms of the translational diffusion coefficient D_T of a monomer, $\langle \boldsymbol{\eta}_i^T(t) \cdot \boldsymbol{\eta}_j^T(t') \rangle = 4D_T \delta_{ij} \delta(t - t')$, in two dimension, and \mathbf{F}_w^i is the interaction with the static obstacle. The solvent-mediated long-range hydrodynamic interactions are neglected for simplicity of the model.

2.1 Simulation Parameters

All the physical parameters are expressed in units of LJ diameter σ , the thermal energy $k_B T$, and the translational diffusion coefficient D_T . The simulation time is in units of $\tau = \sigma^2 / D_T$. The simulation parameters are chosen here as spring constant in the range of $k_s = 10000k_B T / l_0^2$ to $50000k_B T / l_0^2$, $l_0 / \sigma = 1$, $\epsilon / k_B T = 1$, and length of simulation box $L / \sigma = 150$. Further, we express the strength of the active force as a dimensionless quantity called Péclet number Pe , defined as the ratio of active force with thermal force $Pe = f_a l_0 / (k_B T)$. The Péclet number Pe can be equivalently referred to as the directed speed of an active dumbbell; they are related as $v_d = 2PeD_d^0 / \sigma$. The area fraction of the dumbbells is given by $\phi = \frac{N_d \pi \sigma^2}{8[L^2 - \pi R_o^2]}$, here N_d is the number of dumbbells, and R_o is the obstacle radius. The area fraction of the dumbbells is kept fixed throughout the manuscript at $\phi = 0.2$ unless specified in the plots. The obstacle radius is varied in the range of $2.5 - 25$ while keeping ϕ and L fixed. To maintain the same packing fraction of the self-propelled dumbbells for various R_o , we vary the

number of dumbbells from 2500 to 3000. The Péclet number Pe is varied from 0 to 150. The equations of motion (Eq. 3) are integrated by the Euler algorithm with Gaussian distributed random displacements,⁷⁸ with steps ranging from $10^{-4}\tau$ to $2 \times 10^{-6}\tau$. Each simulation point is averaged over at least 10 independent simulation samples.

Our simulation parameters and their considered range can be easily compared with experimental scales^{66,67,69}. Typically, the size of the bacteria and artificial micro-swimmers falls in the range of $1 - 10\mu m$, and their swimming speed lies in the range of $2\mu m/s$ to $28\mu m/s$ ^{16,17,31,35,66}. Considering the size of the active dumbbell in our simulations is $2\mu m$ at room temperature in the fluid viscosity of $\eta_s = 10^{-3}Pa.s$, we can estimate the swim speed using the expression of the Péclet number given as $v_d = 2PeD_d^0/\sigma$, where D_d^0 is the diffusion coefficient of the active dumbbell. This expression provides the active dumbbell's speed in the range of $0\mu m/s - 34\mu m/s$ for the considered simulation range of activity $0 - 150$ (Pe). The obstacle or the micropillar in the previous experimental works are considered nearly of $R_o = 10 - 20\mu m$ ^{31,66,67}. This further makes our simulation window of the aspect ratio R_o/R_d ranging from 2.5 to 12.5, which falls in the range of the experiment scale $2 - 8$ ^{16,17,31,66,67}.

3 Results

The active dumbbells aggregate on the solid interfaces even below the threshold packing of motility-induced phase separation^{18,49}; the static interface and self-propulsion speed nucleate the aggregation. Their aggregation propensity becomes prominent for higher swimming speed, larger curvature radius, and hydrodynamics interactions, which may further enhance wall-induced attractions^{51,68}. Here, we systematically investigate the aggregation behavior of active dumbbells, their orientational ordering and correlations, dynamical behavior on the surface, and the transport behavior of the tracer object as a specific case in the solution of active dumbbells.

3.1 Aggregation on obstacle

The active dumbbells are uniformly distributed at low Péclet numbers with uniform density (n_0). However, as the Péclet number increases, active dumbbells accumulate near the interface, leading to aggregation in the form of a large cluster. This aggregation substantially grows with the activity (Pe). A snapshot of active dumbbells with an obstacle illustrates aggregation behavior near the surface for various Péclet numbers: $Pe = 0, 15, 20,$ and 40 , see Fig. 1 a-d. The average density profile around the obstacle in terms of the color map is also presented in the SI material in Fig. 1.

To gain insights into the non-uniform density profile near the obstacle, we quantify the density distribution function $n(r)$ as a function of radial distance from the center of the obstacle (r/R_o). The spatial variation of the normalized density $n(r)/n_0$ is presented in Fig. 2-a for various Pe at a given $R_o = 15$. As expected for $r/R_o \leq 1$, the density of the active dumbbells is zero inside the obstacle. The figure clearly illustrates the spatial variation of $n(r)/n_0$, which was nearly uniform at relatively low Péclet num-

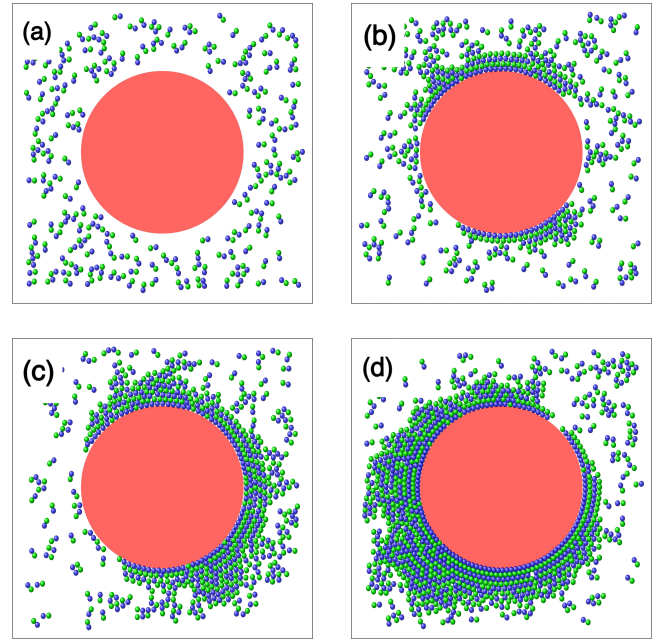


Fig. 1 Simulation Snapshots illustrate aggregation of active dumbbells on the obstacle for various Péclet numbers $Pe = 0, 15, 20,$ and 40 (a-d) at $R_o = 15$. The blue monomer represents the head, the green monomer is the tail of the active dumbbells, and the red disk is the static obstacle.

bers $Pe \leq 10$.

However, as the Péclet number increases ($Pe > 10$), a peak appears on the normalized density distribution $n(r)/n_0$, which eventually saturates for larger Pe . The height and width of this peak exhibit enhancement and subsequent saturation upon increasing the Péclet number. The larger peak height suggests the size of the aggregated cluster grows as depicted in Fig. 2 a. The density profile reaches the bulk value far from the obstacle and remains the same as Fig. 1a-d reflects for all Pe beyond $r/R_o > 2$. The slowdown of the active dumbbells on the surface causes the aggregation and vice versa⁴⁷. For $Pe > 60$, the peak width starts weakly decreasing with augmentation of Pe .

Now, we compute the fraction of active dumbbells accumulated on the obstacle's surface; for this, only those active dumbbells are considered who are already on the surface or part of some cluster on the surface. An active dumbbell is part of an aggregate if the closest distance between any dumbbell's monomer is less than 1.2 ⁷⁹. The computed fraction of active dumbbells $\Phi_c = \langle N_c \rangle / N_d$ is plotted in Fig. 2-b as a function of Pe for various R_o , where $\langle N_c \rangle$ corresponds to the average number of active dumbbells aggregated on the obstacle's surface. Interestingly, the aggregation on the obstacle appears beyond a critical radius ($R_o^c \approx 10$), as Fig. 2 illustrates N_c is nearly zero and does not show significant variation with Pe for $R_o = 5$. For $R_o \geq 10$, the accumulation of active dumbbells is more prominent in the limit of large Pe , as Fig. 2-b depicts.

Similar behavior has been reported in the experiments, where bacterial cells are entrapped by the convex surface only beyond a critical radius⁶⁸. For ($R_o = 10$), the size of aggregation monotonically grows beyond a particular value of Pe before approach-

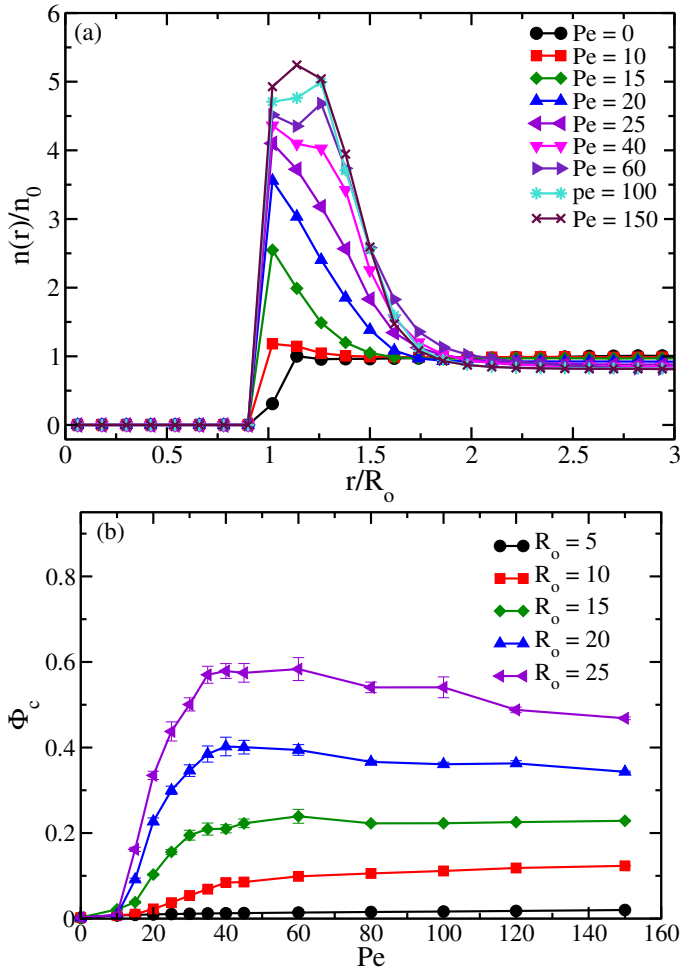


Fig. 2 (a) Normalized density distribution $n(r)/n_0$ of active dumbbells around the center of the obstacle for various Pe at a given $R_o = 15$ as a function of r/R_o . b) The average fraction of active dumbbells onto the obstacle's surface $\Phi_c = \frac{\langle N_c \rangle}{N_m}$ with Péclet number Pe for various R_o .

ing a plateau value in the limit of large Pe . For larger obstacles $R_o = 15, 20,$ and 25 , Fig.2-b displays that the accumulation weakly decreases in the limit of large Pe .

To show the microscopic origin behind the aggregation beyond a critical radius and Pe , we compute the residence time of active dumbbells on the surface as a function of area fraction, incorporating the effect of many-body interactions. The residence time is defined as the average time an active dumbbell spends within a cutoff of 1.5 unit distance from the surface of the circular obstacle. As expected, the residence time is nearly independent of the speed and curvature in the dilute limit; the computed values for various Pe and R_o are shown in SI- Fig.3. Further, the residence time (τ) as a function of the area fraction for various Pe is also shown in Fig. 3, which is nearly unchanged in the dilute limit. However, as the area fraction approaches 0.1, a rapid growth in τ appears as Fig. 3 displays. More importantly, τ has increased nearly two orders of magnitude from its dilute limit. The rapid increase in residence time is attributed to many-body interactions at higher area fractions, indicating the slowdown of rotational diffusion of active dumbbells.

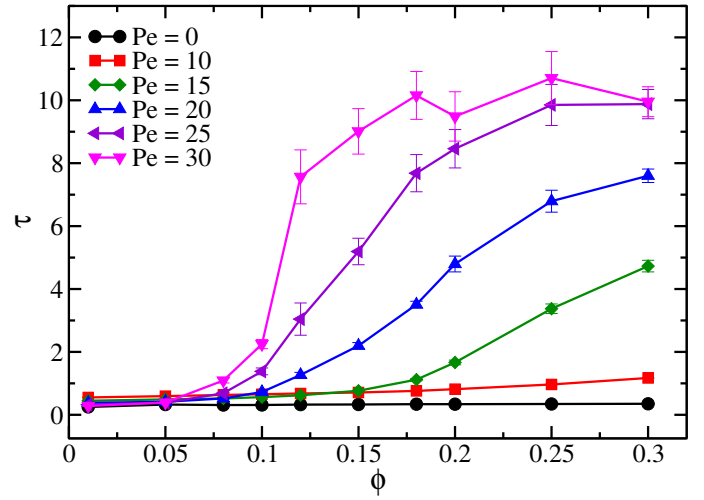


Fig. 3 Plot shows the variation of the residence time τ of active dumbbell as a function of area fraction ϕ for various Pe at $R_o = 15$.

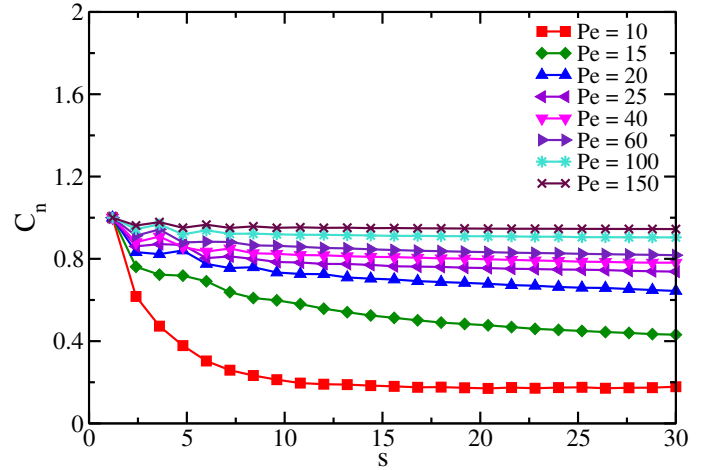


Fig. 4 The alignment correlation function $C_n(s) = \langle \hat{n}_i \cdot \hat{n}_j \rangle$ of active dumbbells around the circumference as a function of arc distance (s) for various Pe , at a given $R_o = 15$.

The aggregation mechanism reported here is similar to the MIPS; when an active dumbbell encounters an obstacle, it remains on the surface up to characteristic time $\tau_c \approx 1/D_r$ before reorientation of its axis due to thermal motion. In the meantime, if other active dumbbells collide with this, they get stuck, leading to a gradual decrease in the rotation of its orientation axis, which further attracts more active dumbbells on this aggregate. This slows down the speed of fast-moving dumbbells and their rotational diffusion, instigating positive feedback beyond a critical Pe . This leads to the phase separation of active dumbbells with a high-density phase on the obstacle surface, coexisting with the low-density phase in the bulk. In summary, we have shown here that aggregation of the active dumbbells on the obstacle occurs only beyond a critical radius and Péclet number due to the dramatic slowdown of the rotational diffusion.

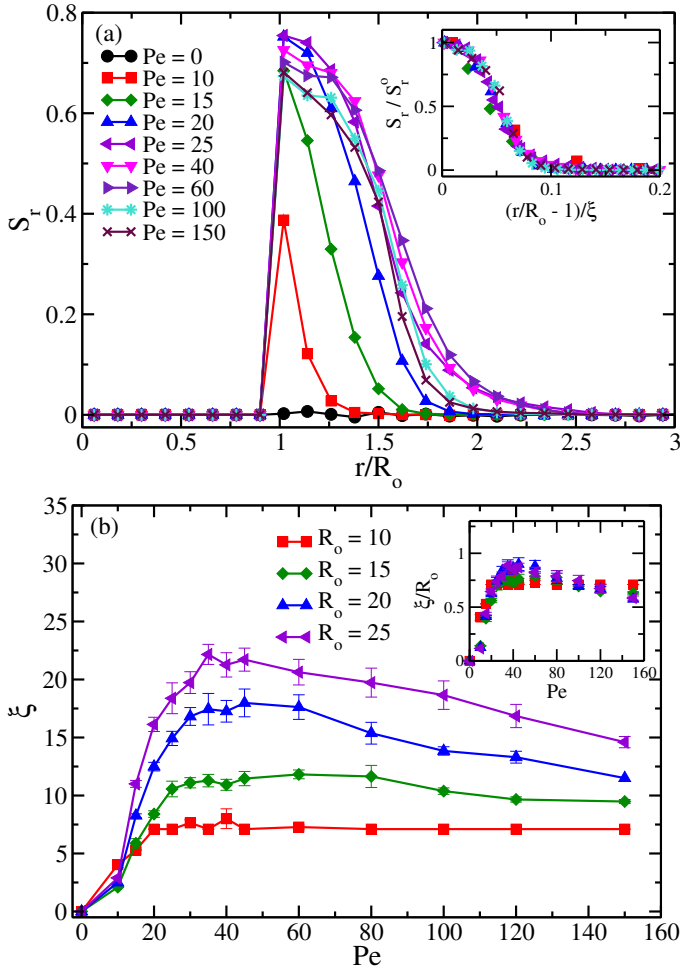


Fig. 5 (a) The local alignment of the active dumbbells w.r.t. normal of the surface ($S_r = \langle -\hat{\mathbf{n}} \cdot \hat{\mathbf{r}} \rangle$) is plotted as a function of radial distance from the center of the obstacle for various Pe and at $R_o = 15$. Inset displays master curve of local alignment parameter S_r/S_r^o as a function of $(r/R_o - 1)/\xi$, where $S_r^o = S_r$ at $r = R_o$. (b) The variation of the correlation length (ξ) is obtained from the radial local alignment parameter S_r , as a function of Pe for various R_o . Inset shows the universal correlation length (ξ/R_o) with the Pe .

3.2 Orientational Ordering

The excluded volume interaction among anisotropic particles along with the surface causes orientational ordering among active dumbbells in the high-density phase⁸⁰; therefore, the polar ordering of the active dumbbells in aggregate is inevitable near the surface. As a result, the ordered phase emerges within the aggregation of active polar dumbbells. Simulation snapshots of Fig. 1 a-d display the tilted alignment and the long-range ordering of active dumbbells along the circumference within a few layers.

We compute the orientational correlation function, which measures the length scale of ordering along its circumference; for this, we use the following expression,

$$C_n(|s - s'|) = \langle \hat{\mathbf{n}}_i(s) \cdot \hat{\mathbf{n}}_j(s') \rangle, \quad (4)$$

where s and s' are the arc positions of the active dumbbells along the circumference of the obstacle, and $\hat{\mathbf{n}}_i$ represents the unit vector of i^{th} active dumbbell, pointing from the tail to head monomer.

The active dumbbells within the first layer, i.e., the cutoff distance 1.5 from the obstacle's surface, are considered to compute this correlation function (C_n). Figure 4 displays alignment correlation C_n decreases rapidly with s for the small Péclet numbers $Pe \leq 20$; however, for $Pe > 20$, the correlation does not decay even 20% of its value for much larger distances. This indicates the presence of the long-range ordering at circumference at higher speeds.

The local alignment of active dumbbells in a radial direction varies with the speed as we go far from the obstacle. To analyze this, we compute the projection of the orientation vector along the obstacle's radial direction. The radial local alignment parameter is defined as $S_r = -\langle \hat{\mathbf{n}} \cdot \hat{\mathbf{r}} \rangle$, where $\hat{\mathbf{r}}$ is the unit radial vector from the center of the obstacle. Figure 5-a displays computed values of S_r as a function of radial distance r for various Pe at a given $R_o = 15$. As expected in equilibrium, aggregation is absent; therefore, active dumbbells are randomly orientated, resulting in S_r being nearly zero everywhere. Once the aggregation sets on the surface, for non-zero activity, S_r increases and exhibits a maximum at the surface. This indicates that alignment becomes prominent for larger Pe at the surface and grows in the radial direction. Strikingly, the height of peak and width weakly decrease for $Pe > 60$ as Fig. 5-a shows. The decrease in the peak and width indicates that the tilt angle increases for $Pe > 60$. Further, as one moves away from the surface, S_r rapidly diminishes, implying the random ordering of active dumbbells in outer layers and bulk.

The length scale over which this orientation remains significant from the surface can be computed from the local radial alignment parameter. In equilibrium, near the wall, the ordering function S_r decays exponentially in dense aggregates as $S_r \approx \exp(-r/\xi)$ ⁸¹. However, the exponential decay is limited only to a short range due to the limited aggregate size. Therefore, to estimate the characteristic correlation length (ξ), we take the distance over which the orientation curve has reduced to 1/e of its maximum value. The estimated correlation length sharply grows with Pe as Fig. 5-b depicts. However, beyond a certain Pe for $R_o < 15$, the correlation length saturates. The saturation of the ξ is a consequence of the finite size aggregate on the obstacle. Besides, for $R_o > 10$, correlation length displays the non-monotonic behavior where the correlation length decreases for the larger Pe , see Fig. 5-b. This observed behavior of the correlation length is consistent with the cluster size and distribution of the active dumbbells around the obstacle, as shown in Fig2-a, and b.

Interestingly, we can find the universal behavior of the correlation length by scaling with the obstacle size (R_o). The inset of Fig. 5-b shows the scaled curve of ξ/R_o with Pe for various R_o . This indicates that the orientational ordering has a length scale of R_o . Moreover, using the correlation length, we can obtain the universal behavior of the local alignment order parameter S_r as presented in the inset of Fig.5-a. This displays the S_r/S_r^o also attains a master curve if presented as a function of $(r/R_o - 1)/\xi$ for various R_o where S_r^o is the value of the S_r at $r = R_o$.

The average global orientational order parameter quantifies the ordering within the system; this can be defined as $S = \langle 2(\hat{\mathbf{n}} \cdot \hat{\mathbf{r}})^2 - 1 \rangle = \langle 2\cos^2(\theta) - 1 \rangle$, where θ represents the orientation of active dumbbell from the normal to obstacle's surface. Figure 6 displays the computed values of global orientational or-

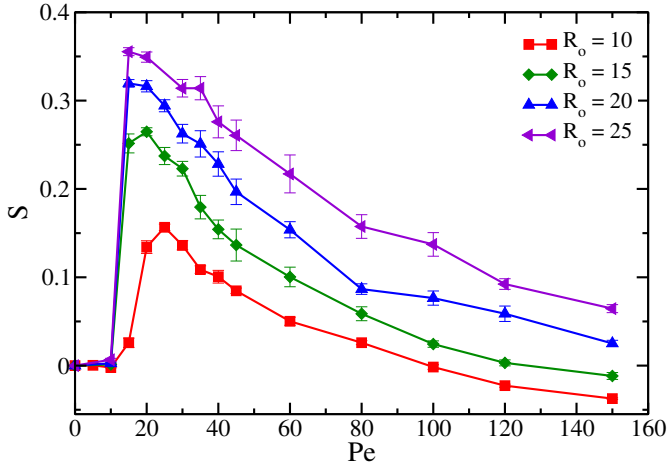


Fig. 6 Average orientational order parameter $S = \langle 2 \cos^2 \theta - 1 \rangle$ as a function of Pe for various R_o . Here θ is the orientation of active dumbbells from the normal to the obstacle's surface.

der parameter S , which increases sharply from zero to a non-zero value beyond a critical value of Pe . This suggests spontaneous ordering and aggregation of active dumbbells on the surface. After approaching a maximum, S starts to descend with Pe . The decrease in global orientational order parameter could be understood from the dynamic behavior of the active dumbbells near the obstacle. The active dumbbells form a tilted array around the circumference of the obstacle; the size of the array increases with Pe . The rotational motion of the aggregation also strengthens with Pe , resulting in a larger tilt angle θ and, consequently, a reduction in the global order parameter (S). The larger tilt angle drives active dumbbells to slide away from the cluster in the limit of large Pe , hence resulting in the decrease of the cluster size and its width for larger activity as has been seen in Fig.2-(a) and (b). This also causes non-monotonic behavior of the correlation length ξ in the same limit.

In summary, domains with locally ordered dense phases are prominent near the surface and coexist with the randomly orientated dilute phase far from the surface. The ordered phase on the surface appears beyond a critical radius R_c and Pe . The dynamical characteristics of the active dumbbells are provided in the subsequent section.

3.3 Dynamics of active dumbbell

The aggregate of active dumbbells spontaneously rotates around the obstacle beyond a critical radius and Péclet number. The dynamic behavior of the active dumbbells is captured in various supporting movies; see SI -Movie 1, 2, and 3 for various Péclet numbers at $R_o = 15$ and Movie 3, 4, and 5 illustrates for various radii at a fixed $Pe = 40$. The persistent rotational motion of the active dumbbells occurs due to orientational ordering and tilted alignment. The rotational motion can also be visualized from the average streamline plot displayed in Fig. 7-a, which illustrates the circulatory flow profile of the velocity vector around the obstacle.

Notably, to demonstrate the direction of the velocity profile \mathbf{v} and local polarity direction \mathbf{p} are not necessarily the same, we

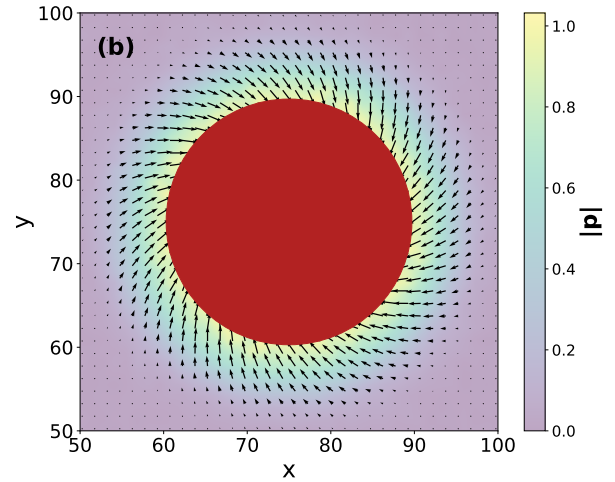
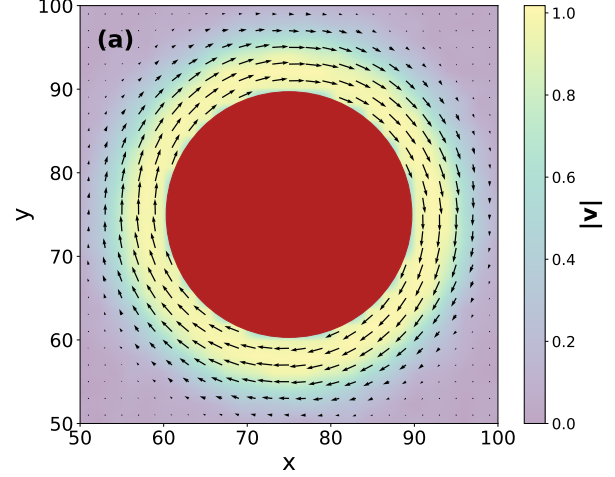


Fig. 7 (a) The normalized local velocity field \mathbf{v} and (b) normalized polarization vector field \mathbf{p} of active dumbbells at a given obstacle radius $R_o = 15$ and activity $Pe = 40$. The color bar indicates the magnitude of the \mathbf{v} and \mathbf{p} in the respective plots.

present local polarization and velocity vectors in Fig. 7 as a vector map. The average vector map \mathbf{p} illustrates the spiral form on the surface, where they all converge on the obstacle at some tilted angle. The vorticity of the velocity field \mathbf{v} and spiral form of the local polarisation vector \mathbf{p} on the surface ensures the rotational motion of the aggregate.

To quantify the rotational motion of the cluster, we compute the tangential component of the velocity of active dumbbells. The tangential speed of active dumbbell w.r.t. the obstacle is $v_t = \langle \mathbf{v} \cdot \hat{\theta} \rangle$, $\hat{\theta}$ is the unit vector in the azimuthal direction from the center of the obstacle.

The variation of the average tangential speed, v_t , of a dumbbell within the aggregate with Péclet number (Pe) is depicted in Fig. 8-a. The tangential speed v_t , for a given R_o beyond $Pe > 10$, grows linearly with Pe . Moreover, it shows weak dependence on the obstacle radius R_o in the limit of small Pe . The slope of v_t weakly decreases with R_o , indicating a decrease of tangential speed (v_t)

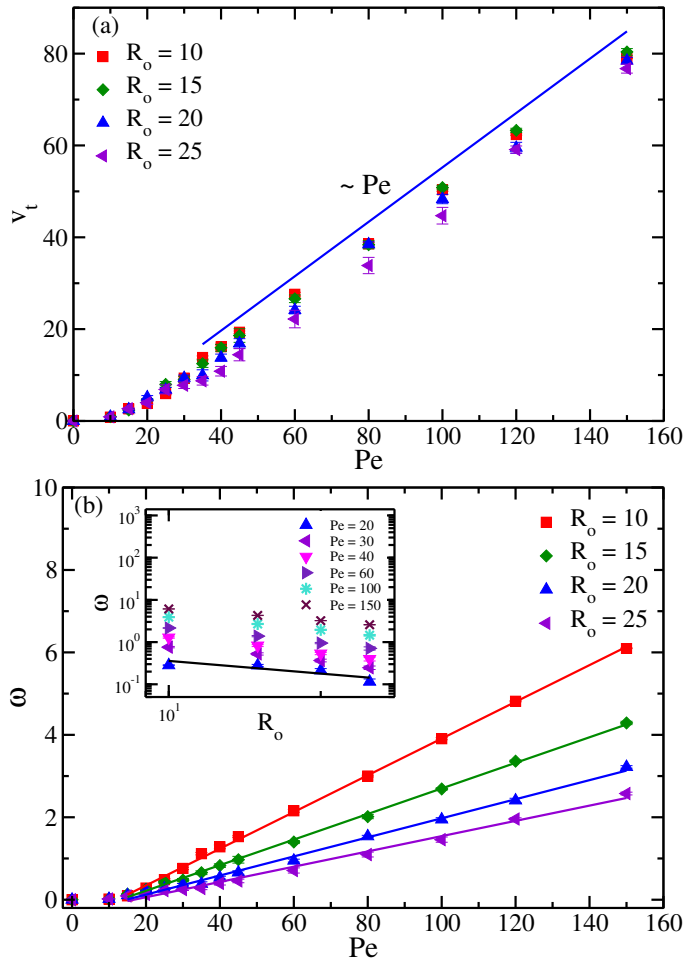


Fig. 8 (a) Variation of the average tangential speed v_t of the active dumbbell as a function of Pe for various R_o . (b) The variation of average angular speed ω of the active dumbbell as a function of Pe for various R_o . This shows tangential and angular speeds linearly grow with Pe in the dense phase. Solid lines show the linear behavior of the angular and tangential speeds. The inset shows the variation of rotational speed ω with R_o for different Pe . The black solid line shows the power behavior of the ω given as $\omega \sim R_o^{-1}$.

in the limit of large Pe for larger radius (R_o). The lower tangential speed for a more considerable radius R_o is due to the large aggregates on the obstacle's surface, which causes a slowdown. This can also be seen in SI Fig. 2-a, where the average directed speed of active dumbbell decreases for larger aggregates. The average angular speed of the active dumbbell can be estimated from the following expression,

$$\omega = \left\langle \frac{1}{|\mathbf{r}|} [\hat{\mathbf{r}} \times \mathbf{v}] \right\rangle. \quad (5)$$

As expected, the estimated angular speed ω also displays a linear increase with Pe , see Fig.8-b. Note that below $Pe < 15$, the spontaneous rotation of the cluster does not appear; thereby, the tangential speed and rotational frequency are nearly zero. Further, we show the dependence of the angular speed ω on the obstacle radius R_o in the inset of Fig. 8-b. The angular speed exhibits power-law variation given as $\omega \sim R_o^{-1}$.

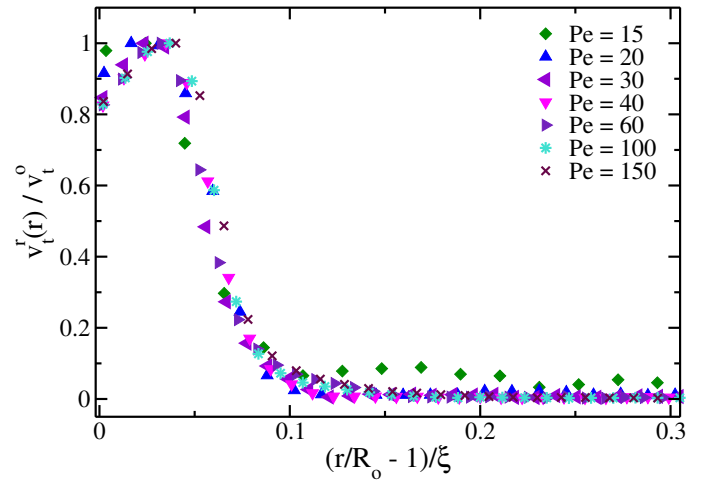


Fig. 9 The scaled tangential speed $v_t^r(r)/v_t^o$ of active dumbbells as a function of scaled linear distance $(r/R_o - 1)/\xi$ from the centre obstacle for various Pe at a given radius $R_o = 15$.

The local tangential speed of the active dumbbell can be presented as a function of the radial distance. Assuming the linear behavior of the angular and tangential speeds, we present the local tangential speed as $v_t^r(r)/v_t^o$ as a function of $(r/R_o - 1)/\xi$, where ξ is correlation length. Remarkably, the scaled quantity $v_t^r(r)/v_t^o$ exhibits universal behavior as depicted in Fig. 9. Here, v_t^o represents the maximum value of $v_t^r(r)$ and exhibits a linear dependence on Pe . Surprisingly, the tangential speed ($v_t^r(r)$) displays a non-monotonic variation, where an increase at shorter distances is followed by a sharp decrease far from the surface, see Fig. 9. The lower tangential speed of the innermost layer results from the dynamic layer coming in contact with the static surface, therefore imposing a higher viscous drag on the inner layers. However, moving away from the surface increases due to a strong alignment correlation in the inner layers. Further away from the surface, The alignment interaction weakens in the cluster; hence, the tangential speed also diminishes in the outer layers.

In summary, we have shown that the front monomer of the dumbbell points toward the obstacle's surface in the aggregate at a certain angle. The locked orientation of the active dumbbells in the cluster applies local force, which translates into torque and causes the cluster to rotate. The rotation of the cluster can be either anticlockwise or clockwise, depending on the tilt angle of the active dumbbells on the surface. For planar confinement, a similar effect has been reported for the sliding motion of hedgehog clusters of self-propelled rods⁸².

3.4 Dynamics of Circular Passive Tracer in Active Medium

We now consider a case where a passive tracer moves in response to thermal and active stresses arising from the medium. The equation of the motion of the passive tracer is governed by the under-damped Langevin equation,

$$M_o \frac{d\mathbf{v}_o}{dt} = -\gamma_o \mathbf{v}_o + \mathbf{F}_w + \mathbf{F}^R. \quad (6)$$

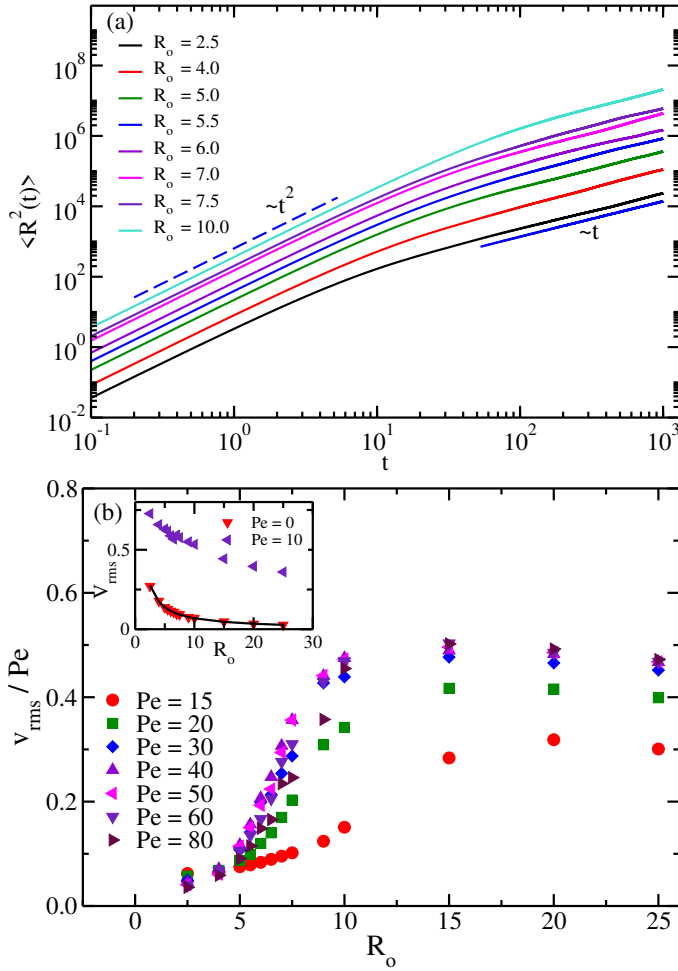


Fig. 10 (a) The plot shows MSD ($\langle R^2(t) \rangle$) of the tracer particle for different radii R_o at a given $Pe = 40$, where blue dashed line indicates ballistic behavior t^2 and solid line shows the diffusive behavior t of the MSD. (b) The normalized average active speed v_{rms}/Pe of the circular tracer particle is presented as a function of its radius R_o for various Pe . The inset shows the average speed at $Pe = 0$ and $Pe = 10$ as a function of R_o . For $Pe = 0$, average speed obeys $v_{rms} \sim R_o^{-1}$ relation shown by solid black line.

Where M_o represents the mass of the tracer particle, \mathbf{v}_o is the velocity, γ_o is the drag, \mathbf{F}_w is the interaction force with the active dumbbells, and \mathbf{F}^R is the random force of a zero mean and correlation given as $\langle \mathbf{F}^R(t) \cdot \mathbf{F}^R(t') \rangle = 4k_B T \gamma_o \delta(t - t')$. The mass of the tracer particle is scaled in units of the mass of the dumbbell's monomer m while keeping mass density fixed, with $M_o = \sigma_o^2 m / (\sigma^2)$. This leads to the choice of the drag coefficient of the tracer being $\gamma_o = \gamma_i \sigma_o / \sigma$, where σ_o is the diameter of the tracer particle. We solve Eq. 6 using the velocity-Verlet algorithm⁸³, with time steps ranging from $10^{-4} \tau$ to $5 \times 10^{-6} \tau$. Other parameters remain same, as listed in the simulation model.

To characterize the dynamics of the passive tracer particle in the active medium, we compute the mean-square-displacement (MSD),

$$\langle R^2(t) \rangle = \langle (\mathbf{r}(t) - \mathbf{r}(0))^2 \rangle. \quad (7)$$

As displayed in Fig. 10-a, The MSD of the passive tracer in the active medium attains the superdiffusive behavior, indicated by

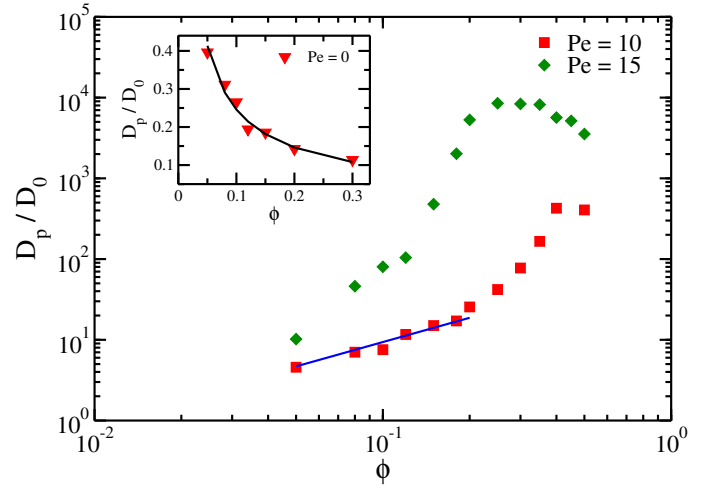


Fig. 11 The effective diffusivity D_p/D_0 of the tracer particle is shown as a function of area fraction ϕ for different Pe at a fixed $R_o = 15$, where the diffusion coefficient of the passive tracer is given as, $D_0 = k_B T / \gamma_o$. The blue line shows a linear fit for lower values of ϕ . The inset shows the effective diffusivity of a tracer particle D_p/D_0 decreases monotonically with the increase in ϕ for the passive bath ($Pe = 0$).

$\langle R^2(t) \rangle \sim \langle v_o^2 \rangle t^2$, which is followed by the diffusive behavior in the long time limit ($\langle R^2(t) \rangle = 4D_p t$) for various values of R_o , at $Pe = 40$. Where D_p is the effective diffusion coefficient of the tracer particle of the radius R_o .

From the MSD curves, we estimate the average speed of the tracer particle in the superdiffusive regime using the following expression $\langle R^2(t) \rangle = \langle v_o^2 \rangle t^2$. The average speed of the tracer particle can be computed $v_{rms} = \sqrt{\langle v_o^2 \rangle}$, which is displayed in Fig. 10-b for various Pe .

For the passive system, i.e., $Pe = 0$, the speed of the tracer particle decreases with R_o following the relation $v_{rms} \sim R_o^{-1}$. This is intuitive as we know the speed of a tracer $v_{rms} \sim M_o^{-1/2}$, that leads to $v_{rms} \sim R_o^{-1}$. For $Pe = 0$, a solid line in the inset of Fig. 10-b establishes the speed decrease with the inverse of the obstacle radius.

There is a noticeable shift in the behavior of v_{rms} with Pe in the active medium; surprisingly, the speed of tracer particle increases with R_o which is a very different in passive medium. More-importantly, for the $Pe \geq 30$, v_{rms} speed increases with R_o latter it decreases at higher packing, see Fig.10-b. The increase in the speed of the tracer particle is a consequence of the increase in the heterogeneous aggregation of the active dumbbells on the surface of the tracer particle with the size of the obstacle, see Fig.1 and 2. This can also be seen in the SI- movies 6 and 7 for Péclet numbers $Pe = 10$ and 40 at fixed $R_o = 15$. For $R_o > 15$, as expected, the speed of the tracer decreases due to larger viscous drag. Interestingly, beyond $Pe \geq 30$, all the curves of the v_{rms} superimpose on top of each other once they are scaled with the Péclet number (Pe) as Fig.10-b displays the universal behavior of v_{rms}/Pe with R_o .

In the large time regime, the MSD of the tracer particle assumes diffusive behavior as displayed in Fig. 10-a. We estimate the effective diffusion coefficient by varying the area fraction of the active

dumbbells using the relation $\langle R^2(t) \rangle = 4D_p t$. The computed values of the effective diffusivity $D_p(\phi)$ as a function of area fraction ϕ are depicted in Fig. 11. As expected in the passive bath, the diffusion coefficient monotonically decreases with ϕ , see in the inset of Fig. 11. Interestingly, The effective diffusion coefficient of the tracer particle in the active bath with ϕ linearly increases in the dilute regime, followed by a rapid upsurge up to $\phi < 0.3$, unlike the passive medium. Notably, it has increased by over four orders of magnitude. Further, an increase in $\phi > 0.3$ causes a decrease in D_p . Thus, effective diffusivity also exhibits a non-monotonic behavior with ϕ ; as Fig. 11 illustrates. The linear growth of D_p with ϕ in the dilute regime and non-monotonic feature is consistent with experimental observations^{74–77}. In summary, the increase in the effective diffusion results from active noise in the dilute and intermediate packing fractions. The decrease of the effective diffusivity at higher density is due to the slowdown of the speed of the active dumbbell and the formation of larger aggregation in the regime.

4 Conclusion

This article presented a comprehensive study of active dumbbells in the presence of a circular static obstacle. We have shown that beyond a critical obstacle radius $R_o^c \approx 10$ and Péclet number, active dumbbells aggregate on the surface of the static obstacle. This aggregate spontaneously rotates along the obstacle circumference. The average tangential speed and rotational frequency of active dumbbells within the aggregation increase linearly with the Péclet number. The rotation of the aggregate emerged from the torque imposed by the jammed orientation of active dumbbells in the cluster. We have also shown that the local tangential speed of the active dumbbells reflects the non-monotonic behavior as one moves away from the surface. More importantly, all the curves show universal behavior. The tangential speed initially increases but sharply decreases in the outer layers. The former is a consequence of the jamming of active dumbbells on the innermost layer of aggregate, while in the outer layers, active dumbbells fluctuate; therefore, tangential speed decreases.

To understand the microscopic origin of the surface aggregation, we also analyzed the residence time (τ) of active dumbbells in the proximity of the obstacle as a function of area fraction and its speed. A rapid increase in the residence time is shown with a slight increase in concentration. This non-linear increase in the residence time is attributed to the slowdown of rotational diffusion, which leads to the aggregation and, thereby, alignment of the active dumbbells on the surface. This provides the microscopic origin of the aggregation and rotational motion and its qualitative dependence on the curvature radius and the activity.

In addition, we have shown that the average polarization vector \mathbf{p} differs from the velocity vector profile. The former has a spiral-like profile, while the latter displays a vortex form. The observed distinct directions of the local polarization vector with the velocity field have also been reported in studies of active dumbbells in the absence of solid interface¹⁸; this mandates the direction of the velocity profile, and the polarization vector needs to be treated separately in the microscopic theories^{49,80}. Furthermore, our study also reveals a strong orientational ordering

among active dumbbells within the aggregate and along the circumference of the obstacle. The active dumbbells align themselves on the surface at a certain orientational angle from the normal to the surface; this angle further decreases with obstacle radius and increases with Pe . Moreover, the correlation length of the orientational alignment demonstrates a long-range ordering, with the correlation length becoming as large as the size of the aggregate. Additionally, we have shown the universal behavior of local alignment (S_r) and local tangential speed (v_r') in terms of the correlation length (ξ) that itself grows linearly with R_o .

Our simulations demonstrate a particular case when obstacles are free to move in response to active and thermal forces. The tracer particle displays directed motion. Moreover, the tracer particle's speed increases with its size, followed by a decrease in the limit of the larger radius beyond a critical Péclet number, despite the increase in the viscous drag with size. Furthermore, we have also shown that the effective diffusivity of the tracer particle displays the non-monotonic behavior with the density of the active dumbbells in the active medium. This non-intuitive increase in the speed and diffusion coefficient is a consequence of a large aggregation of active dumbbells on the surface of the tracer particle compared to smaller ones. The non-monotonic behavior of the effective diffusion of the tracer is also observed in the bacterial solution⁷⁴. This indicates the transport of the relatively bigger particles in the active medium is relatively easier, which can have potential applications in the targeted delivery of the drugs and extracting work from the active medium^{22,84}.

Previous studies have revealed that non-uniform aggregation of active particles on the surface of the asymmetric tracer that guides to directed^{85–88} as well as rotational motion^{7,89,90}. Recent work has shown that such motion is not restricted to asymmetric tracer particles; a symmetric tracer with critical porosity in the active solution also exhibits directed motion⁸⁴. On the contrary, our study extends this behavior to a smooth, symmetric system. It unveils that the directed motion can be achieved for the relatively bigger-sized symmetric tracer particle in the solution of active dumbbells. Our results will be helpful in elucidating the behavior of the microbial dynamics in microfabricated devices^{22,91,92}.

The surface-driven aggregation and vortex formation have promising applications in controlling the turbulent dynamics of active suspensions^{3,22,91,93–95}. The hydrodynamic interactions are ignored for the model's simplicity, albeit they may have a considerable impact on the entrapment of the microswimmers^{70,71,96}. However, their influence is not expected to alter the qualitative behavior of the collective dynamics of the active dumbbells described in this study. Our model considers a simple model that ignores the influence of deformation of the microswimmer in the dense medium. This may play a critical role in the aggregation and entrapment near interface^{71,96,97}. To closely align with the experimental investigations of bacterial dynamics, a periodic array of obstacles, incorporating the hydrodynamic interactions, may be considered in future works^{16,22,66}.

5 Acknowledgments

SPS and CHT acknowledge financial support from the DST-SERB Grant No. CRG/2020/000661 and UGC, respectively. The com-

putational facilities of IISER Bhopal and Paramshivay NSM at IIT-BHU are highly acknowledged.

Notes and references

- 1 J. Elgeti and G. Gompper, *The European Physical Journal Special Topics*, 2016, **225**, 2333–2352.
- 2 W. Poon, *Physics of complex colloids*, 2013, **184**, 317–377.
- 3 C. Dombrowski, L. Cisneros, S. Chatkaew, R. E. Goldstein and J. O. Kessler, *Physical review letters*, 2004, **93**, 098103.
- 4 K. Ishimoto and E. A. Gaffney, *Scientific Reports*, 2018, **8**, 15600.
- 5 N. Kumar, R. K. Gupta, H. Soni, S. Ramaswamy and A. Sood, *Physical Review E*, 2019, **99**, 032605.
- 6 M. C. Marchetti, J.-F. Joanny, S. Ramaswamy, T. B. Liverpool, J. Prost, M. Rao and R. A. Simha, *Reviews of modern physics*, 2013, **85**, 1143.
- 7 R. Di Leonardo, L. Angelani, D. Dell’Arciprete, G. Ruocco, V. Iebba, S. Schippa, M. P. Conte, F. Mecarini, F. De Angelis and E. Di Fabrizio, *Proceedings of the National Academy of Sciences*, 2010, **107**, 9541–9545.
- 8 M. E. Cates, *Reports on Progress in Physics*, 2012, **75**, 042601.
- 9 S. Ramaswamy, *Annu. Rev. Condens. Matter Phys.*, 2010, **1**, 323–345.
- 10 J. Elgeti, R. G. Winkler and G. Gompper, *Reports on progress in physics*, 2015, **78**, 056601.
- 11 A. Zöttl and H. Stark, *Journal of Physics: Condensed Matter*, 2016, **28**, 253001.
- 12 J.-T. Kuhr, F. Rühle and H. Stark, *Soft Matter*, 2019, **15**, 5685–5694.
- 13 H.-P. Zhang, A. Be’er, E.-L. Florin and H. L. Swinney, *Proceedings of the National Academy of Sciences*, 2010, **107**, 13626–13630.
- 14 G. Liu, A. Patch, F. Bahar, D. Yllanes, R. D. Welch, M. C. Marchetti, S. Thutupalli and J. W. Shaevitz, *Physical review letters*, 2019, **122**, 248102.
- 15 Y. Fily, A. Baskaran and M. F. Hagan, *Soft matter*, 2014, **10**, 5609–5617.
- 16 H. Wioland, F. G. Woodhouse, J. Dunkel, J. O. Kessler and R. E. Goldstein, *Physical review letters*, 2013, **110**, 268102.
- 17 E. Lushi, H. Wioland and R. E. Goldstein, *Proceedings of the National Academy of Sciences*, 2014, **111**, 9733–9738.
- 18 A. Suma, G. Gonnella, D. Marenduzzo and E. Orlandini, *Europhysics Letters*, 2014, **108**, 56004.
- 19 E. Lauga and T. R. Powers, *Reports on Progress in Physics*, 2009, **72**, 096601.
- 20 Y. Peng, Z. Liu and X. Cheng, *Science advances*, 2021, **7**, eabd1240.
- 21 J. Dunkel, S. Heidenreich, K. Drescher, H. H. Wensink, M. Bär and R. E. Goldstein, *Physical review letters*, 2013, **110**, 228102.
- 22 D. Nishiguchi, I. S. Aranson, A. Snezhko and A. Sokolov, *Nature communications*, 2018, **9**, 4486.
- 23 L. Hall-Stoodley, J. W. Costerton and P. Stoodley, *Nature reviews microbiology*, 2004, **2**, 95–108.
- 24 N. Keller, J. Bruchmann, T. Sollich, C. Richter, R. Thelen, F. Kotz, T. Schwartz, D. Helmer and B. E. Rapp, *ACS applied materials & interfaces*, 2019, **11**, 4480–4487.
- 25 Rothschild, *Nature*, 1963, **198**, 1221.
- 26 D. Woolley, *REPRODUCTION-CAMBRIDGE-*, 2003, **126**, 259–270.
- 27 T. Kaya and H. Koser, *Biophysical journal*, 2012, **102**, 1514–1523.
- 28 E. Lauga, W. R. DiLuzio, G. M. Whitesides and H. A. Stone, *Biophysical journal*, 2006, **90**, 400–412.
- 29 J. Hill, O. Kalkanci, J. L. McMurry and H. Koser, *Physical review letters*, 2007, **98**, 068101.
- 30 B. R. Si, P. Patel and R. Mangal, *Langmuir*, 2020, **36**, 11888–11898.
- 31 V. R. Krishnamurthi, N. Harris, A. Rogers, M. Zou and Y. Wang, *Colloids and Surfaces B: Biointerfaces*, 2022, **209**, 112190.
- 32 K. Chaithanya and S. P. Thampi, *Physical Review Fluids*, 2021, **6**, 083101.
- 33 E. Secchi, A. Vitale, G. L. Miño, V. Kantsler, L. Eberl, R. Rusconi and R. Stocker, *Nature communications*, 2020, **11**, 2851.
- 34 A. T. Brown, I. D. Vladescu, A. Dawson, T. Vissers, J. Schwarz-Linek, J. S. Lintuvuori and W. C. Poon, *Soft matter*, 2016, **12**, 131–140.
- 35 T. Bhattacharjee and S. S. Datta, *Nature communications*, 2019, **10**, 2075.
- 36 E. Irani, Z. Mokhtari and A. Zippelius, *Physical Review Letters*, 2022, **128**, 144501.
- 37 A. Dehkharghani, N. Waisbord and J. S. Guasto, *Communications Physics*, 2023, **6**, 18.
- 38 T. Jakuszeit and O. A. Croze, *arXiv preprint arXiv:2309.04326*, 2023.
- 39 A. Creppy, E. Clément, C. Douarche, M. V. D’angelo and H. Auradou, *Physical Review Fluids*, 2019, **4**, 013102.
- 40 T. Bhattacharjee and S. S. Datta, *Soft Matter*, 2019, **15**, 9920–9930.
- 41 D. Shrestha, J. Ou, A. Rogers, A. Jereb, D. Okyere, J. Chen and Y. Wang, *Colloids and Surfaces B: Biointerfaces*, 2023, **222**, 113128.
- 42 K. Beppu, Z. Izri, J. Gohya, K. Eto, M. Ichikawa and Y. T. Maeda, *Soft Matter*, 2017, **13**, 5038–5043.
- 43 J. Stenhammar, A. Tiribocchi, R. J. Allen, D. Marenduzzo and M. E. Cates, *Physical review letters*, 2013, **111**, 145702.
- 44 Y. Fily and M. C. Marchetti, *Physical review letters*, 2012, **108**, 235702.
- 45 G. S. Redner, M. F. Hagan and A. Baskaran, *Biophysical Journal*, 2013, **104**, 640a.
- 46 J. Bialké, H. Löwen and T. Speck, *Europhysics Letters*, 2013, **103**, 30008.
- 47 M. E. Cates and J. Tailleur, *Europhysics Letters*, 2013, **101**, 20010.
- 48 M. E. Cates and J. Tailleur, *Annu. Rev. Condens. Matter Phys.*, 2015, **6**, 219–244.
- 49 A. Suma, G. Gonnella, G. Laghezza, A. Lamura, A. Mossa and

- L. F. Cugliandolo, *Physical Review E*, 2014, **90**, 052130.
- 50 S. Das and R. Chelakkot, *Soft Matter*, 2020, **16**, 7250–7255.
- 51 S. K. Anand and S. P. Singh, *Soft Matter*, 2019, **15**, 4008–4018.
- 52 X.-L. Wu and A. Libchaber, *Physical review letters*, 2000, **84**, 3017.
- 53 L. Angelani, C. Maggi, M. Bernardini, A. Rizzo and R. Di Leonardo, *Physical review letters*, 2011, **107**, 138302.
- 54 P. Dolai, A. Simha and S. Mishra, *Soft Matter*, 2018, **14**, 6137–6145.
- 55 F. Jose, S. K. Anand and S. P. Singh, *Soft Matter*, 2021, **17**, 3153–3161.
- 56 R. S. Yadav, C. Das and R. Chakrabarti, *Soft Matter*, 2023, **19**, 689–700.
- 57 P. Kumar and R. Chakrabarti, *Physical Chemistry Chemical Physics*, 2023, **25**, 1937–1946.
- 58 B. Bhattacharjee and D. Chaudhuri, *Soft matter*, 2019, **15**, 8483–8495.
- 59 E. Sesé-Sansa, D. Levis and I. Pagonabarraga, *Physical Review E*, 2021, **104**, 054611.
- 60 S. R. McCandlish, A. Baskaran and M. F. Hagan, *Soft Matter*, 2012, **8**, 2527–2534.
- 61 H. Wioland, E. Lushi and R. E. Goldstein, *New Journal of Physics*, 2016, **18**, 075002.
- 62 M. Bär, R. Großmann, S. Heidenreich and F. Peruani, *Annual Review of Condensed Matter Physics*, 2020, **11**, 441–466.
- 63 A. Zöttl and H. Stark, *The European Physical Journal E*, 2013, **36**, 1–10.
- 64 A. Zöttl and H. Stark, *Physical review letters*, 2014, **112**, 118101.
- 65 S. K. Anand and S. P. Singh, *The European Physical Journal E*, 2021, **44**, 1–10.
- 66 P. Chopra, D. Quint, A. Gopinathan and B. Liu, *Physical Review Fluids*, 2022, **7**, L071101.
- 67 S. E. Spagnolie, G. R. Moreno-Flores, D. Bartolo and E. Lauga, *Soft Matter*, 2015, **11**, 3396–3411.
- 68 O. Sipos, K. Nagy, R. Di Leonardo and P. Galajda, *Physical review letters*, 2015, **114**, 258104.
- 69 D. Takagi, J. Palacci, A. B. Braunschweig, M. J. Shelley and J. Zhang, *Soft Matter*, 2014, **10**, 1784–1789.
- 70 J.-x. Pan, H. Wei, M.-j. Qi, H.-f. Wang, J.-j. Zhang, K. Chen *et al.*, *Soft Matter*, 2020, **16**, 5545–5551.
- 71 Z. Mokhtari, T. Aspelmeier and A. Zippelius, *Europhysics Letters*, 2017, **120**, 14001.
- 72 A. Deblais, T. Barois, T. Guerin, P.-H. Delville, R. Vaudaine, J. S. Lintuvuori, J.-F. Boudet, J.-C. Baret and H. Kellay, *Physical review letters*, 2018, **120**, 188002.
- 73 A. Costanzo, R. Di Leonardo, G. Ruocco and L. Angelani, *Journal of Physics: Condensed Matter*, 2012, **24**, 065101.
- 74 A. E. Patteson, A. Gopinath, P. K. Purohit and P. E. Arratia, *Soft matter*, 2016, **12**, 2365–2372.
- 75 G. Mino, T. E. Mallouk, T. Darnige, M. Hoyos, J. Dauchet, J. Dunstan, R. Soto, Y. Wang, A. Rousselet and E. Clement, *Physical review letters*, 2011, **106**, 048102.
- 76 A. Jepson, V. A. Martinez, J. Schwarz-Linek, A. Morozov and W. C. Poon, *Physical Review E*, 2013, **88**, 041002.
- 77 K. C. Leptos, J. S. Guasto, J. P. Gollub, A. I. Pesci and R. E. Goldstein, *Physical Review Letters*, 2009, **103**, 198103.
- 78 D. L. Ermak and J. A. McCammon, *The Journal of chemical physics*, 1978, **69**, 1352–1360.
- 79 S. D. Stoddard, *Journal of Computational Physics*, 1978, **27**, 291–293.
- 80 P.-G. De Gennes and J. Prost, *The physics of liquid crystals*, Oxford university press, 1993.
- 81 M. Doi, *Liquid crystals*, Oxford University Press, 2013.
- 82 H. H. Wensink and H. Löwen, *Phys. Rev. E*, 2008, **78**, 031409.
- 83 M. P. Allen and D. J. Tildesley, *Computer simulation of liquids*, Oxford university press, 2017.
- 84 S. Das, S. Ghosh and R. Chelakkot, *Physical Review E*, 2020, **102**, 032619.
- 85 C. Bechinger, R. Di Leonardo, H. Löwen, C. Reichhardt, G. Volpe and G. Volpe, *Reviews of Modern Physics*, 2016, **88**, 045006.
- 86 S. Mallory, C. Valeriani and A. Cacciuto, *Physical Review E*, 2014, **90**, 032309.
- 87 A. Kaiser, K. Popowa, H. Wensink and H. Löwen, *Physical Review E*, 2013, **88**, 022311.
- 88 F. Smallenburg and H. Löwen, *Physical Review E*, 2015, **92**, 032304.
- 89 L. Angelani, R. Di Leonardo and G. Ruocco, *Physical review letters*, 2009, **102**, 048104.
- 90 A. Sokolov, M. M. Apodaca, B. A. Grzybowski and I. S. Aranson, *Proceedings of the National Academy of Sciences*, 2010, **107**, 969–974.
- 91 H. Wioland, F. G. Woodhouse, J. Dunkel and R. E. Goldstein, *Nature physics*, 2016, **12**, 341–345.
- 92 P. Pietzonka, É. Fodor, C. Lohrmann, M. E. Cates and U. Seifert, *Physical Review X*, 2019, **9**, 041032.
- 93 M. M. Genkin, A. Sokolov, O. D. Lavrentovich and I. S. Aranson, *Physical Review X*, 2017, **7**, 011029.
- 94 S. Zhou, *Lyotropic chromonic liquid crystals: From viscoelastic properties to living liquid crystals*, Springer, 2017.
- 95 K. Qi, E. Westphal, G. Gompper and R. G. Winkler, *Communications Physics*, 2022, **5**, 49.
- 96 Y. Wang, Y.-w. Gao, K. Chen *et al.*, *Physical Chemistry Chemical Physics*, 2022, **24**, 23779–23789.
- 97 J. Palacci, S. Sacanna, A. Abramian, J. Barral, K. Hanson, A. Y. Grosberg, D. J. Pine and P. M. Chaikin, *Science advances*, 2015, **1**, e1400214.

Supplementary Information: Collective dynamics of active dumbbells near circular obstacle

Chandranshu Tiwari* and Sunil P. Singh†
 Department of Physics,
 Indian Institute of Science Education and Research,
 Bhopal 462 066, Madhya Pradesh, India

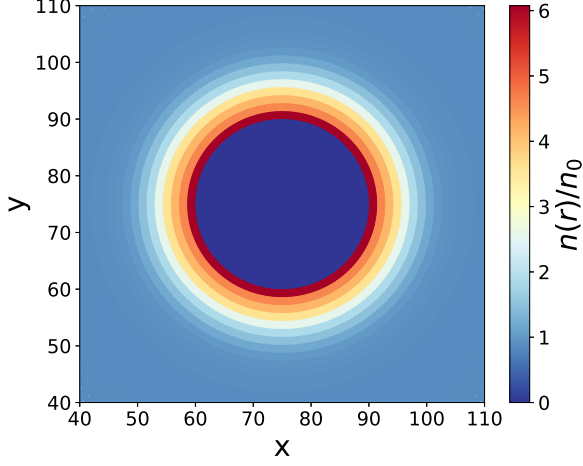


FIG. 1. The color map reflects the average density of active dumbbells around the obstacle of radius $R_o = 15$ at a given $Pe = 40$. The central dark blue patch depicts the circular obstacle with zero density of the active dumbbells. The color bar shows the variation of the normalized density around the obstacle's surface. Only a portion of the simulation box is displayed to clarify the density profile.

I. NORMALISED DENSITY MAP

The normalized average density profile of active dumbbells, represented by $n(r)/n_0$ shown in Figure 1, exhibits a distinctive pattern. Near the obstacle's surface, $n(r)/n_0$ has a maximum value, signifying the highest concentration of active dumbbells. As one moves away from the surface, $n(r)/n_0$ gradually decreases, and far from the surface, the density of the active dumbbells approaches unity, i.e., the bulk value. This indicates that near the surface, the density profile is significantly higher than the bulk, displaying an aggregation of active dumbbells on the obstacle's surface.

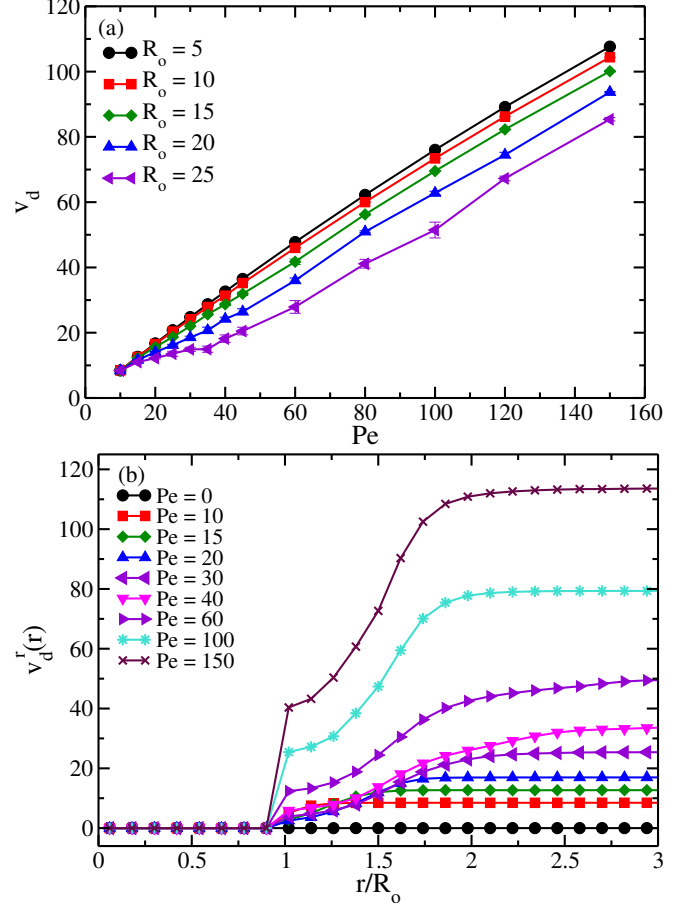


FIG. 2. (a) The variation of average directed speed, as a function of Pe for different radii (R_o). (b) The distribution of average directed speed $v_d^r(r)$ from the center of obstacle for various Pe at a given $R_o = 15$.

II. DIRECTED SPEED

To provide detailed insights into the dynamics of a single active dumbbell, we analyze the average directed speed of a dumbbell in the presence of a static obstacle. The average directed speed (v_d) is defined as the average projection of the velocities of active dumbbells along their axes of orientations, i.e., $v_d = \langle \mathbf{v} \cdot \hat{\mathbf{n}} \rangle$. Figure 2-a displays the average directed speed of a dumbbell as a function of Péclet number (Pe) for various obstacle radii. Directed speed also grows linearly with Pe at a fixed obstacle radius R_o ; however, as R_o increases, the

* chandranshu21@iiserb.ac.in

† spsingh@iiserb.ac.in

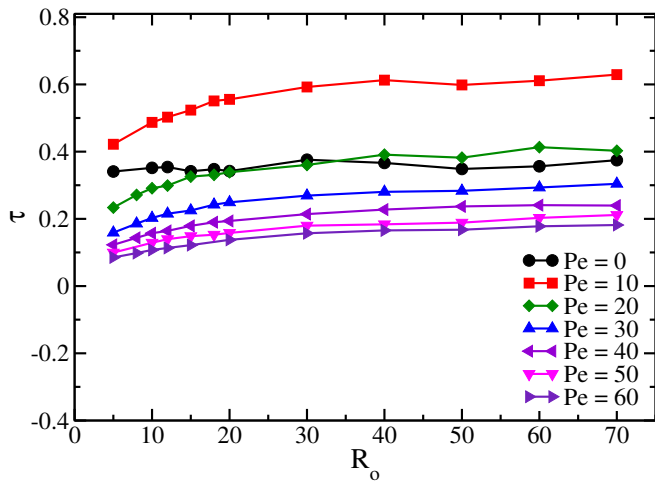


FIG. 3. Variation of the residence time τ as a function of R_o for various Pe .

$v_d - Pe$ curve shifts downwards, reflecting the decrease in the directed speed. This is because aggregation size becomes more prominent for higher R_o , as discussed in the manuscript. Consequently, within these aggregates, the active dumbbells slow down considerably. The increased aggregation size contributes to a reduction in speeds; as a result, it leads to decay in the directed speed for larger R_o .

Nevertheless, despite this slowdown, active dumbbells form ordered jammed structures around the circumference of the surface that generate torque on the cluster, therefore having the significant tangential speed to make them rotate around the obstacle.

Furthermore, we probe the average directed speed $v_d^r(r)$ as a function of radial distance r from the center of an obstacle for various Pe at fixed obstacle radius $R_o = 15$. As expected, for the passive system $Pe = 0$, the average directed speed is zero; therefore, $v_d^r(r)$ remains zero at all distances, see Fig. 2-b. While for low activity ($Pe < 10$), the directed speed $v_d^r(r)$ near the obstacle's surface and far from them is nearly the same due to lack of dense aggregation on the surface, in this limits the density of active dumbbells is everywhere roughly same as in bulk phase. However, for $Pe \geq 15$ aggregation of the dumbbell sets on the surface, the speed of dumbbells is significantly reduced near the surface, as illustrated in Fig. 2-b. The directed speed monotonically grows as we go far from the surface until it reaches a plateau corresponding to the speed of active dumbbells in the homogeneous bulk phase.

III. RESIDENCE TIME

Now, we present the residence time of an active dumbbell on the obstacle's surface in the dilute concentration as a function of radius R_o and active speed Pe . We place a randomly oriented active dumbbell on the obstacle's

surface to compute this time. Then, we measure the average duration a dumbbell spends within a cutoff radius of 1.5 from the surface of a circular obstacle, called here residence time τ . This calculation is averaged over 2500 randomly oriented particles on the obstacle's surface.

Figure 3 illustrates the variation of the residence time τ as a function of obstacle radius R_o for different Péclet numbers Pe . For a passive system, i.e., $Pe = 0$, the residence time τ remains constant across all R_o values. However, for active systems, the residence time weakly increases with R_o for all Pe . As Pe increases, the curve shifts downward, indicating that the residence time decreases for larger Pe . This reduction in residence time at higher Pe values is attributed to active particles exiting in the cutoff region at higher speeds, primarily when oriented away from the surface. In summary, our finding indicates that, in the dilute limit, the residence time of active dumbbells demonstrates only a weak dependence on both curvature radius (R_o) and Péclet number (Pe). Further, the effect of the concentration of the active dumbbells leads to dramatic increases of τ , as discussed in the main manuscript.

IV. SUPPLEMENTARY MOVIES

Here, we provide various supporting movies to illustrate the collective dynamics of active dumbbells around the static obstacle and the dynamic behavior of a tracer particle in the medium of active dumbbells.

Movie S1: The movie shows the dynamics of the active dumbbells at Péclet number $Pe = 10$ at a given obstacle radius $R_o = 15$. Only the central portion of the simulation box is presented for clarity.

Movie S2: The movie shows the dynamics, aggregation, and rotation of the active dumbbells on the surface of an obstacle at Péclet number $Pe = 20$ at a given radius $R_o = 15$. Only the central portion of the simulation box is presented for clarity.

Movie S3: The movie shows the dynamics, aggregation, and rotation of the active dumbbells on the surface of an obstacle at Péclet number $Pe = 40$ at a given radius $R_o = 15$. Only the central portion of the simulation box is presented for clarity.

Movie S4: The movie shows the dynamics of the active dumbbells at Péclet number $Pe = 40$ at a given obstacle radius $R_o = 5$. Only the central portion of the simulation box is presented for clarity.

Movie S5: The movie shows the dynamics, aggregation, and rotation of the active dumbbells on the surface of an obstacle of radius $R_o = 10$ at Péclet number $Pe = 40$. Only the central portion of the simulation box is presented for clarity.

Movie S6: The movie illustrates the dynamic behavior of a tracer particle of radius $R_o = 15$ at $Pe = 10$ in the solution of the active dumbbells.

Movie S7: The movie illustrates the dynamic behavior of a tracer particle of radius $R_o = 15$ at $Pe = 40$ in the solution of the active dumbbells.